ORIGINAL ARTICLE

Global and local performances of a tubular micro-pulsating heat pipe: experimental investigation

Luca Cattani[1] · Pamela Vocale[1] · Fabio Bozzoli[1,2] · Matteo Malavasi[1] · Luca Pagliarini[1] · Naoko Iwata[3]

Abstract

Heat exchanger optimization is mandatory in almost any industrial application. Thanks to their performances, the Pulsating Heat Pipes (PHPs) are a very interesting application. Micro-PHPs, which are defined as PHPs with a tube that has a hydraulic diameter < 500 µm, have shown big advantages in terms of their ability to dissipate high heat fluxes, their reduced size, and their low weight. However, the great majority of the works that investigate the thermal behavior of micro-PHPs only deal with the average performance of the system, usually represented in terms of global thermal resistance of the device. Our study aims to begin to fill this lack by investigating the local thermal behavior of a typical multi-turn micro-PHP. A micro-PHP characterized by seven turns and realized with a stainless-steel pipe was investigated. It was positioned in a vertical position, with the evaporator at the bottom, and it was partially loaded with HFC-134a. The studied micro-PHP is tubular, while almost the totality of the micro-PHPs investigated to date are constituted by microchannels engraved in silicon-based wafer, and they present a great potential in terms of three-axis flexibility compared to the flat micro-PHPs that are usually investigated. To highlight the different thermal functioning of each turn, an infrared camera was used to acquire the local temperature distributions on the wall of the PHP condenser. It was found that the best performance was reached for a filling ratio of 46% and for a heat input ranging between 1.9–3.7 W. To thoroughly study the pulsating behavior of the proposed PHP, the dominant frequencies were investigated by performing a wavelet analysis. The results allow the identification of different flow regimes, such as start-up, non-persistent oscillating flow (0.05–0.6 Hz; $Q_{net} < 2.3$ W), and quasi-periodic oscillating flow (0.6–1.5 Hz; $Q_{net} = 2.8$–4.7 W). Eventually, the results highlight that the approach proposed herein can provide worthy evidence about the fluid motion inside the PHP, thereby allowing to overcome the limits introduced by the adoption of transparent materials for the direct flow visualization or by the invasive insertion of pressure sensors, particularly in devices with such small dimensions.

Abbreviations

a	Wavelet scale dilation parameter
A	Heat transfer area m^2
f	Frequency
h	Convective heat transfer coefficient W/m^{2}K
L	Length m
Q	Heat power W
R_t	Thermal resistance K/W
s	Thickness m
T	Temperature °C
t	Time s

Greek Symbol

ε	Efficiency parameter defined in Eq. (6)
λ	Thermal conductivity W/(m•K)
η	Non-dimensional time
τ	Wavelet time translation parameter
ψ	Wavelet mother

Subscript

c	Condenser
e	Evaporator
env	Environment
ref	Reference

✉ Luca Cattani
luca.cattani1@unipr.it

1 Department of Engineering and Architecture, University of Parma, Parco Area delle Scienze 181/A, 43124 Parma, Italy

2 SITEIA.PARMA Interdepartmental Centre, University of Parma, Parco Area delle Scienze 181/A, 43124 Parma, Italy

3 Research and Development Directorate, Japan Aerospace Exploration Agency, 2-1-1 Sengen, Tsukuba, Ibaraki 3058505, Japan

1 Introduction

Device miniaturization, together with the assessment of more efficient components, is one of the main scientific and technological challenge of the last decades. The miniaturization of components produces an increase of the heat fluxes per unit surface area and imposes a need for new technological solutions [1, 2]. With these premises, a solution that shows great potential is pulsating heat pipes (PHPs) [3], which consist of a capillary loop, partly charged with a fluid, and which are characterized by alternating heating and cooling areas. The PHPs represent one of the more promising two-phase passive heat transfer devices, due to their unique features such as their construction simplicity, low costs, capability of dissipating high heat fluxes, and self-driven fluid motion—which means no need for mechanical/electrical power and moving parts. The inner diameter of the PHPs must be small enough that surface tension forces dominate gravitational forces and that an alternance of liquid slugs and vapor plugs can be formed by capillary action. Despite their unique advantages, the thermo-fluid dynamics governing the internal two-phase oscillating flow is highly complex, because many processes such as capillary actions, inertia forces, and phase changes are involved; therefore, the behavior of these devices has not yet been fully understood. To analyze and thoroughly comprehend the essential working principles of PHPs, many studies have been carried out in recent years [4–11].

Micro-PHPs are defined as PHPs with a tube that has a hydraulic diameter < 500 μm [4]. Micro-PHPs are mainly adopted in electronic equipment cooling, including laptop computers, smartphones, transistors, and audio amplifiers. Micro-PHPs are also employed in spacecraft cooling due to their low weight. Another application related to space engineering may be controlling the body temperature of astronauts. In fact, due to their deformability, micro-PHPs could be applied directly onto the thermal straps of the spacecraft and the astronaut's spacesuit [12, 13].

Analogously to PHP, micro-PHPs are also characterized by thermal performance which is primarily influenced by the oscillating motion of the working fluid. To investigate the characteristic features of the oscillatory flow, some authors have performed flow visualizations [14–18] and frequency analyses [15]. The studies currently available in the literature that investigate locally the characteristics of oscillating motion in a micro-PHP are limited to the fluid-dynamic working principles; furthermore, they do not directly concern the local thermal behavior, even if these two physics are strictly connected. Indeed, as with PHPs, the great majority of publications on the thermal behavior of micro-PHPs assess the average performance of the system, which is usually represented in terms of global

thermal resistance of the device [16–21]. However, as was the case for the fluid-dynamics characteristics deduced from the flow visualization, the knowledge of local thermal phenomena may be of crucial importance.

The current work proposes, to the authors' knowledge, one of the first local analyses of the thermal behavior of a multi-turn micro-PHP. The aim is to provide useful and quantitative information for better optimization and comprehension of the fundamental physical mechanisms ruling the behavior of these devices. The micro-PHP external wall temperature distributions were measured in the condenser area by a high-speed and high-resolution infrared camera, and these distributions were analyzed to study the local influence of the pulsating flow on the thermal performance of the proposed micro-PHP. The adoption of an infrared camera to measure the temperature of the PHP offers the opportunity to avoid the main problems that are present in most of the studies in which temperatures are measured by contact sensors (e.g., thermocouples, thermo-resistors), namely, poor reliance of probes' location and sensor disturbance on the measured temperature. These issues are increasingly relevant when the investigated device is characterized by small dimensions, such as the analysis of the micro-PHPs.

An additional element of novelty in our study is the fact that the studied micro-PHP is tubular, whereas the micro-PHPs in the majority of studies are not round tube but microchannels engraved in silicon-based wafer [15–18, 20, 21]. The micro-PHP with thin metallic tube has hardly been studied so far, despite its potentials for three-axis flexibility and high heat transport performance.

Adopting the temperature maps acquired by infrared camera also makes it possible to perform a wide frequency analysis of the thermal oscillations occurring in the whole device, which could provide an interesting alternative to the classical methods for investigating the pulsations that characterize the motion in these devices. Indeed, this technique overcomes the limitations introduced by the adoption of transparent materials for direct flow visualization (i.e., disturbance induced by the junctions, low thermal conductivity, costs) or by the invasive insertion of pressure sensors, particularly in devices with such small dimensions.

One of the most important outcomes of the frequency analysis is the opportunity to identify the dominant frequency that, as described by Xu et al. [22], represents the frequency corresponding to an energy peak in the power spectrum.

To carry out a frequency analysis in PHPs, different techniques has been adopted, such as short-time Fourier transform [23], Hilbert–Huang transform [23], fast Fourier transform [24], and the wavelet coefficient [25].

However, it must be highlighted that the Fourier transform (FT) is not suitable in the analysis of signals that

present strong variations of the components in frequency over time, as is the case in micro-PHPs [25]. The short-time Fourier transform (STFT) is also unsuitable, because the length of the floating window in this approach is fixed [25]. The length of the window, which is decisive for a better frequency resolution, must be short enough to assert the hypothesis of stationarity of the signal and to be able to apply the FT. Since the temperature signals in micro-PHPs are highly variable, it is not possible to find a window length that allows a good resolution in frequency and that allows maintaining the hypothesis of stationarity of a portion of the signal. To overcome these limitations, wavelet analysis can be carried out, as performed by Zhao et al. [25]. This technique enables adapt the length of the window to extrapolate information related to a specific frequency range [26].

In the present work, we present a PHP fabricated with an extra-thin metallic tube [12] with an internal diameter of 0.32 mm and filled with HFC-134a. This device was chosen because in a preliminary investigation [13] it was proved to be an ideal representative case of micro-PHPs, allowing to combine deformability and compactness with excellent heat transfer performance.

To characterize the local performance of the tested micro-PHP, several heating powers and filling ratios were investigated. To highlight the different thermal behavior of each turn, an infrared camera was used to acquire the local temperature distributions on the wall of the entire PHP. To thoroughly study the pulsating behavior of the proposed PHP, the dominant frequencies were investigated by wavelet analysis.

2 Experimental setup

The micro-PHP under investigation consisted of three main parts: the evaporator, condenser, and adiabatic section; each section was 50 mm in length, as shown in Figs. 1. The device was realized with a stainless-steel pipe with internal and external diameters of 0.32 mm and 0.52 mm, respectively. The tube was bent by hand using a cylindrical metal bar for support. Bending a pipe with a small diameter, especially when the bending radius is small, causes flattening—or, in the worst case, breakage—of the bent part. Before fabricating the PHP, a tube with the same diameter as the PHP was put into the trials of bending, and the minimum bending radius of the tube, which does not flatten noticeably, was 3 mm. When measuring the outer diameter of the tips of the bent PHP part, the section remains circular within a tolerance of 2%; therefore, the tubes are not considered flattened in the bent part. The tube was joined end-to-end (i.e., closed loop structure) and was bent into seven turns.

The micro-PHP was positioned in a vertical position (90°), with the evaporator at the bottom; in this section, tubes were
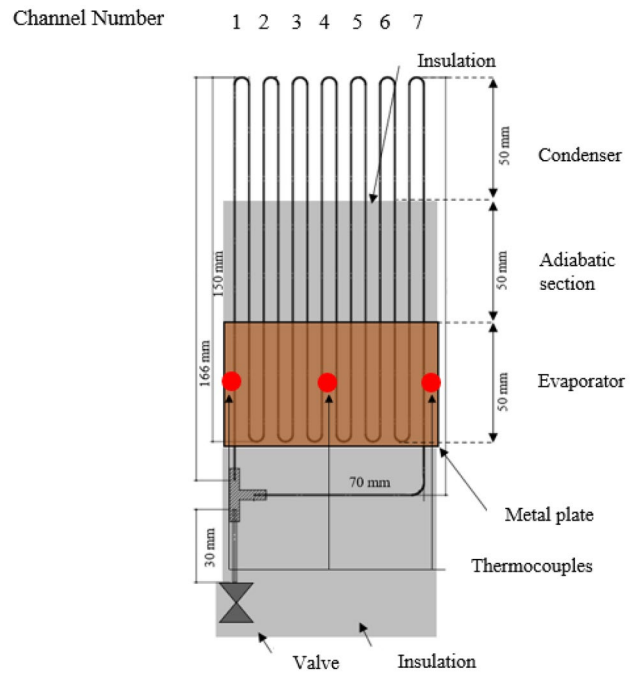

Fig. 1 Sketch of the investigated device

fixed to a 3-mm metal plate by aluminum tapes on whose back side a polyimide sheet heater was pasted. During the system assembly, the tube was pressed onto the heating plate; due to the plasticity of the thin tube, this procedure allowed a perfect adjustment of the tube to the plate, yielding a uniform contact thermal resistance. The temperature uniformity in the evaporator obtained with this configuration has been verified with a preliminary test, finding a maximum temperature difference over the plate of 0.1 K at a 3 W power input. The heating power was provided at the evaporator in the range 0.1 – 4.7 W, and it corresponds to an average heat flux at the pipe wall between 1.6×10^2 W/m^2 and 7.5×10^3 W/m^2. Each heat input
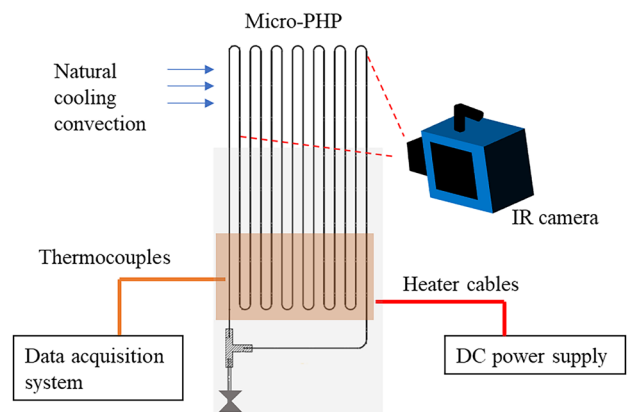

Fig. 2 Schematic of the experimental setup

step was maintained for several minutes to reach the pseudo-steady state. The pipes in the cooling section were exposed to the atmospheric air and were cooled by natural convection. Figure 1 shows the numbering of the turns. The evaporator section, the heating plate, the adiabatic section, and the valve were insulated on both sides by means of 2-cm in width of expanded polyurethane.

After being vacuumed, the micro-PHP was partially charged with HFC-134a through the valve shown in Fig. 1. To evaluate the impact of the filling on the thermal behavior of the micro-PHP, several FRs in the range of 30–82 vol% were tested. The filling ratio (*FR*) is defined as the fraction by volume of the heat pipe, which is initially filled with the liquid (evaluated at room temperature). The fluid volume is calculated from the liquid density at room temperature and from the fluid mass, which is obtained by measuring the weight of the micro-PHP with and without the fluid. Moreover, the empty micro-PHP was tested to show the comparison with the purely conductive mode.

The temperature of the evaporator was measured through three type-T thermocouples affixed onto the metal plate by means of aluminum tape. The temperature distribution at the condenser was acquired by means of a FLIR SC7000 infrared camera (see Fig. 2) with a 640×512 pixels detector array, which allowed thermal images to be captured with an acquisition frequency of 18 Hz. Its thermal sensitivity, as reported by the instrument manufacturer, was 20 mK at 303 K, while its accuracy was ± 1 K. The camera was placed 40 cm directly across from the PHP in order to be able to capture the entire condenser.

In correspondence of the condenser section, the tubes were covered with a thin layer of black paint that permits a uniform and high surface emissivity without altering the heat conduction in the pipe wall. The viewing angle was limited to less than $\pm 30°$; therefore, the surface could be treated as a diffuse grey emitter [27].

To determine the actual value of the coating emissivity, a set of tests was performed by shooting a tubular target at different known temperatures, which yielded a value of 0.95 ± 0.01.

To verify that the thermal resistance between the heater and the pipe was uniform, a preliminary experiment was executed by adopting the empty PHP and verifying that the three thermocouples at the evaporator presented the same values and that the temperature distribution detected at the condenser with the infrared camera was uniform. Given that both conditions were satisfied, the thermal resistance between the heater and the pipe was considered uniform.

3 Data processing

3.1 Thermal resistance

The first step of our study evaluated the average performance of the micro-PHP by computing the average thermal

resistance for each turn and then for the whole device. This calculation was defined as follows:

$$R_{t,i} = \frac{T_e - T_{c,i}}{Q_{net}} \tag{1}$$

where $R_{t,i}$ is the thermal resistance of the *ith* turn, Q_{net} is the net heat power provided at the heating section, T_e is the evaporator temperature, and $T_{c,i}$ is the condenser temperature of the *i-th* turn. Precisely, Q_{net} is the electrical heat input reduced by the heat losses to the surroundings, T_e is obtained by averaging the values of the three thermocouples placed on the metal plate, and $T_{c,i}$ is found by averaging the temperature measured by the infrared camera in the central area of the *i-th* turn. The heat losses to the surroundings were calculated as follows:

$$Q_l = A_p \cdot \frac{\lambda_p}{s_p} \cdot \left(T_e - T_{env} \right) \tag{2}$$

where λ_p and s_p were the thermal conductivity and thickness of the expanded polyurethane layer, respectively, A_p represents the surface area of the expanded polyurethane layer, and T_{env} is the environment temperature.

The evaporator and condenser temperature were the average of the measured values over a 60-s period.

The limited variation in the evaporator temperature (< 0.1 K) among the values measured by the sensors proved the good impact of the metal plate in terms of temperature uniformity at the evaporator.

The uncertainty in thermal resistance was evaluated with the propagation of error method [28]; the maximum uncertainty on the thermal resistance was $\pm 10\%$, $\pm 5\%$, and $\pm 3\%$ at low ($Q_{net} < 1$ W), medium (1 W $< Q_{net} < 3$ W), and high heating powers ($Q_{net} > 3$ W), respectively. Finally, the uncertainty of the filling ratio was approximately 5%.

3.2 Frequency analysis

One crucial distinctive characteristic of PHPs is their pulsating motion. The heat exchange in PHPs arises due to self-exciting pulsation that is powered by high-speed oscillating pressure waves generated by the alternance of nucleate boiling and the ensuing condensation of the internal fluid [29]. Indeed, the working fluid pulsations in the axial direction of the pipe allow heat transfer from the evaporator to the condenser. The driving force is represented by the heat provided at the evaporator, which enhances the pressure of the vapor plugs in this section. The pressure increment thrusts the neighboring vapor plugs and liquid slugs in the direction of the condenser, which is characterized by a lower pressure.

Several methods have been employed to investigate this oscillatory behavior in PHPs [23–25]. The oscillating motion

of the working fluid between the evaporator and the condenser section is characterized by a variable pulsation frequency [25]. For this reason, it is customary to define the fluid pulsation frequency in PHPs as a peak in the power spectrum (i.e., the dominant frequency of a specific dataset) [22]. Recently, among the techniques adopted for frequency analysis, wavelet analysis achieved resounding interest [30, 31]. As defined in [31], a wavelet function can be any real or complex-valued function $\psi(t) \in L$ that fulfills the subsequent acceptability requirement:

$$C_\psi = \int_{-\infty}^{\infty} |\hat{\psi}(f)|^2 |f|^{-1} df < \infty \tag{3}$$

where $\hat{\psi}(f)$ is the Fourier transform of $|\psi(t)|$. To ensure the reversibility of the transform, C_ψ must be a finite quantity; actually, this hints that $\psi(t)$ has zero mean value. Under this acceptability requirement, the wavelet transform $W_y(a, \tau)$ of a signal $y(t)$ can be calculated as follows [26, 30]:

$$W_y(a, \tau) = \frac{1}{\sqrt{a}} \int_{-\infty}^{\infty} y(t) \psi^* \left(\frac{t - \tau}{a} \right) dt \tag{4}$$

where a and τ are the wavelet scale dilation and time translation parameters, respectively, and the superscript * denotes the complex conjugate.

Practically, wavelets are a group of self-similar mathematical functions that are adopted to approximate more complex functions via super positioning principles and to permit the division of a signal into distinct frequency and time components. Wavelet analysis is strictly connected to Fourier analysis, since both allow a certain function to be represented as the summation of basis functions. The basis adopted in the Fourier analysis are sine trigonometric functions, while in wavelet analysis it is a specific group of self-similar, orthonormal basis functions that are identified in time and space [32]. These functions are all created from one primary function known as the mother wavelet. The wavelet basis is obtained by translation and expansion of the mother wavelet.

These operations can be expressed by the time translation τ and scale dilation a parameters, respectively. Wavelet analysis on a signal detected over time is carried out with a contracted, higher-frequency form of the mother wavelet, whereas frequency analysis is implemented by means of a translation of the same wavelet [32].

The selection of the proper wavelet mother relies on the features of the analyzed signal. Morlet wavelet ψ was demonstrated to be a good choice for transient localization [26, 33] and is defined as follows:

$$\psi(\eta) = \frac{1}{\sqrt{\pi}} e^{-\frac{\eta^2}{2}} e^{i f_0 \eta} \tag{5}$$

where η is the non-dimensional time and f_0 is the non-dimensional frequency.

A wavelet function has its specific central frequency f_0 at every single scale, and the scale a is inversely proportional to that frequency. A big scale corresponds to a low frequency, providing overall evidence of the signal. Small scales are related to high frequencies, giving thorough signal details. By varying the scale a, the mother wavelet is narrowed and expanded. The changing in scale a modifies the non-dimensional frequency f_0 and the window size [34].

On the other hand, the time translation parameter τ delineates the position of the wavelet in time, and the wavelet can be shifted over the signal by varying τ [32].

The components $W_\psi(a, \tau)$ are wavelet coefficients, with each corresponding to a scale (a) and a time point (τ) [34]. The signal energy is normalized at every scale by dividing the wavelet coefficients by $1/\sqrt{a}$. This guarantees that the wavelets have the same energy at every scale [35].

Specifically, for the Morlet wavelet, the frequency f is associated with the scales a by the relation $f = f_0/a$. Even if the scale a is typically adopted in lieu of the frequency when discussing the wavelet analysis results in our study, the outcomes are discussed in terms of frequency in order to facilitate comprehension by readers, since the concept of frequency is usually more familiar than the concept of scales.

The assessment of the continuous wavelet transform (Eq. 5) is typically achieved by assuming discrete values for the a and τ parameters. The ensuing wavelet coefficients are termed wavelet series [34]. To calculate all the different wavelet series, discrete Fourier transforms are habitually utilized [26]. Nevertheless, this approach generates error in the determination of the power spectrum of the wavelet; this inconvenience is related to the fact that the Fourier transform hypothesizes that the data are periodic, thereby creating problems in the power spectrum reconstruction at the beginning and end of every finite-length time series [26, 36].

One remedy is to fill out the end of the time series with zeroes before performing the wavelet transform, after which the zeroes are removed [26, 37]. Padding with zeroes creates gaps at the borders and, for larger scales, reduces the amplitude close to the boundaries as more zeroes are inserted [26, 36].

The area in which zero-filling influences the assessment of the wavelet spectrum is named the cone of influence and is described as the zone where the wavelet power decreases by a factor of e^{-2} due to discontinuities at the edge [26]. Consequently, the areas under the cone of influence are inclined to border effects. Therefore, to correctly analyze wavelet coefficients, the cone of influence must be excluded.

Usually, wavelet analysis outcomes are discussed in terms of the magnitude scalogram, which is defined as the power connected to every frequency over the test interval, and in

terms of the power spectrum, which represents the time integral for every frequency of the magnitude scalogram.

More precisely, the scalogram, which is a measure of the energy distribution of the signal ($|W_y(a,\tau)|^2$) allows the determination of the main oscillation frequencies of the investigated oscillations (i.e., the frequencies characterized by the highest power over time), whereas the power spectrum identifies the frequency with the highest power within the whole observation window, and it is obtained from the integration in time (i.e., for each scale/frequency) of the wavelet spectra. According to [30, 32], the dominant frequency is considered the greatest value of the wavelet power spectrum.

3.3 Analysis validation with synthetic data

To test the effectiveness of the wavelet analysis to find the dominant frequencies of the discontinuous pulsating phenomena in micro-PHPs, four representative signals varying with time t were analyzed. Two sine functions and two square waves were tested, as shown in Fig. 3. These signals were chosen because they present periodicity, shape, and change in frequency and amplitude comparable to those of the experimental temperature signals investigated in the present work.

The results in terms of scalogram and power spectrum are reported in Fig. 4 for all the functions considered. The cones of influence for the analyzed signals are indicated by grey regions in Fig. 4. Accordingly, to properly evaluate the wavelet coefficients, only the data outside the cone of influence must be considered. As expected, the maximum energy distribution occurs at the characteristic frequency of the analyzed signal. By analyzing the power spectrum for the sine functions (Fig. 5a and c), it was observed that both sine functions presented a peak at f = 0.159 Hz (i.e., the dominant frequency), which was identical to the frequency of the original signals [$f = 1/(2\pi)$].
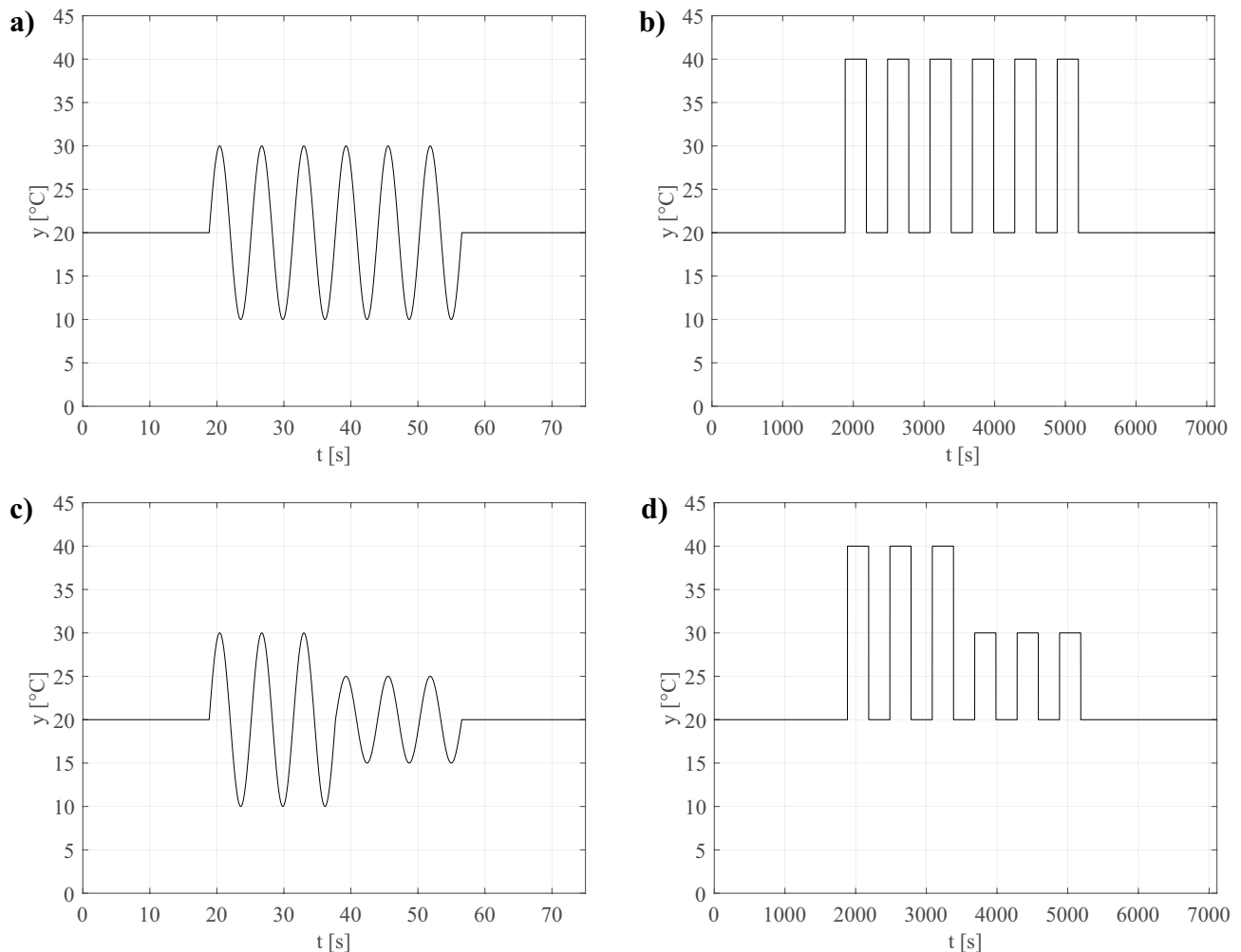

Fig. 3 Analyzed signals: **a**) sine function; **b**) square wave; **c**) sine function with two different amplitudes; **d**) square wave with two different amplitudes
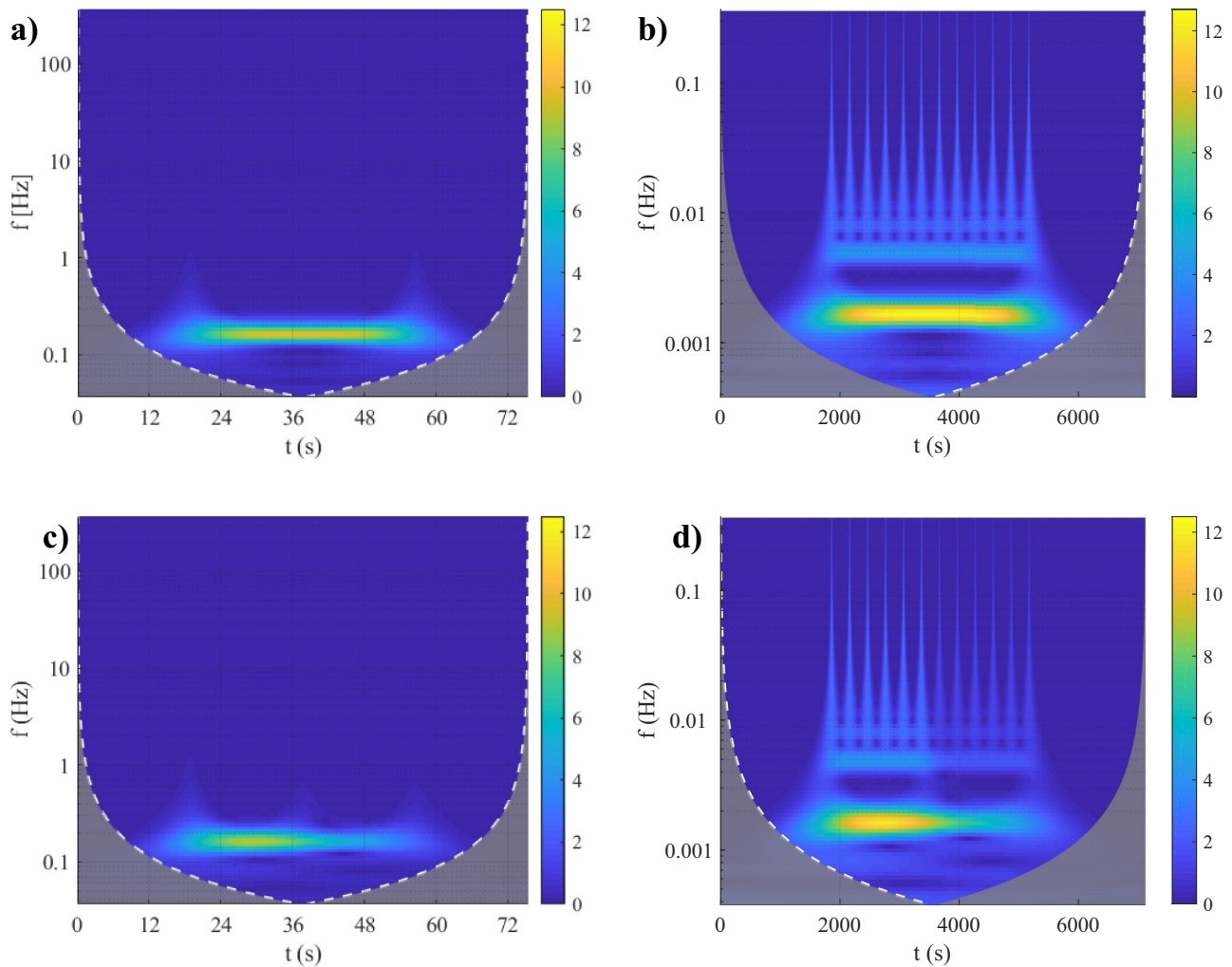
Fig. 4 Scalograms: **a**) sine function; **b**) square wave; **c**) sine function with two different amplitudes; **d**) square wave with two different amplitudes

With respect to the square waves, the dominant frequency for both signals was 0.0017 Hz (Fig. 5b and d), which was identical to the frequency of the original signals. Therefore, it can be concluded that the adopted wavelet enables the proper characterization of the analyzed signals, thereby confirming the effectiveness of the adopted methodology.

4 Results and discussion

4.1 Thermal resistance

Figure 6 shows the evaporator and condenser temperatures for the representative case of $FR = 46\%$ for all heating powers. Each temperature step corresponds to a different heat input that was held for a period of time sufficient to achieve the pseudo-steady state. As concerns the condenser temperature, the data presented in Fig. 6 are the average of the values measured on the central pipe (i.e., turn 4 in Fig. 1) by means of the infrared camera.

For the same value of the filling ratio, $FR = 46\%$ was reported as the average thermal resistance as a function of the heat input (Fig. 7). Of note is that, since this value of filling ratio is usually considered in the range of the optimal filling ratios [3, 6], it was deeply investigated.

The thermal resistance of the micro-PHP investigated here presents a similar trend to that observed in different micro-PHPs [18, 38] and in other PHPs [39, 40]. At low heat inputs, the thermal resistance is high and begins to drops as the power input increases until the device reaches an operating range in which the thermal resistance is characterized by low values. This trend can be explained by considering that at a low heat input, the fluid shows an absent or limited oscillating behavior; whereas, at higher heating powers, the movement of the fluid increases and progressively involves
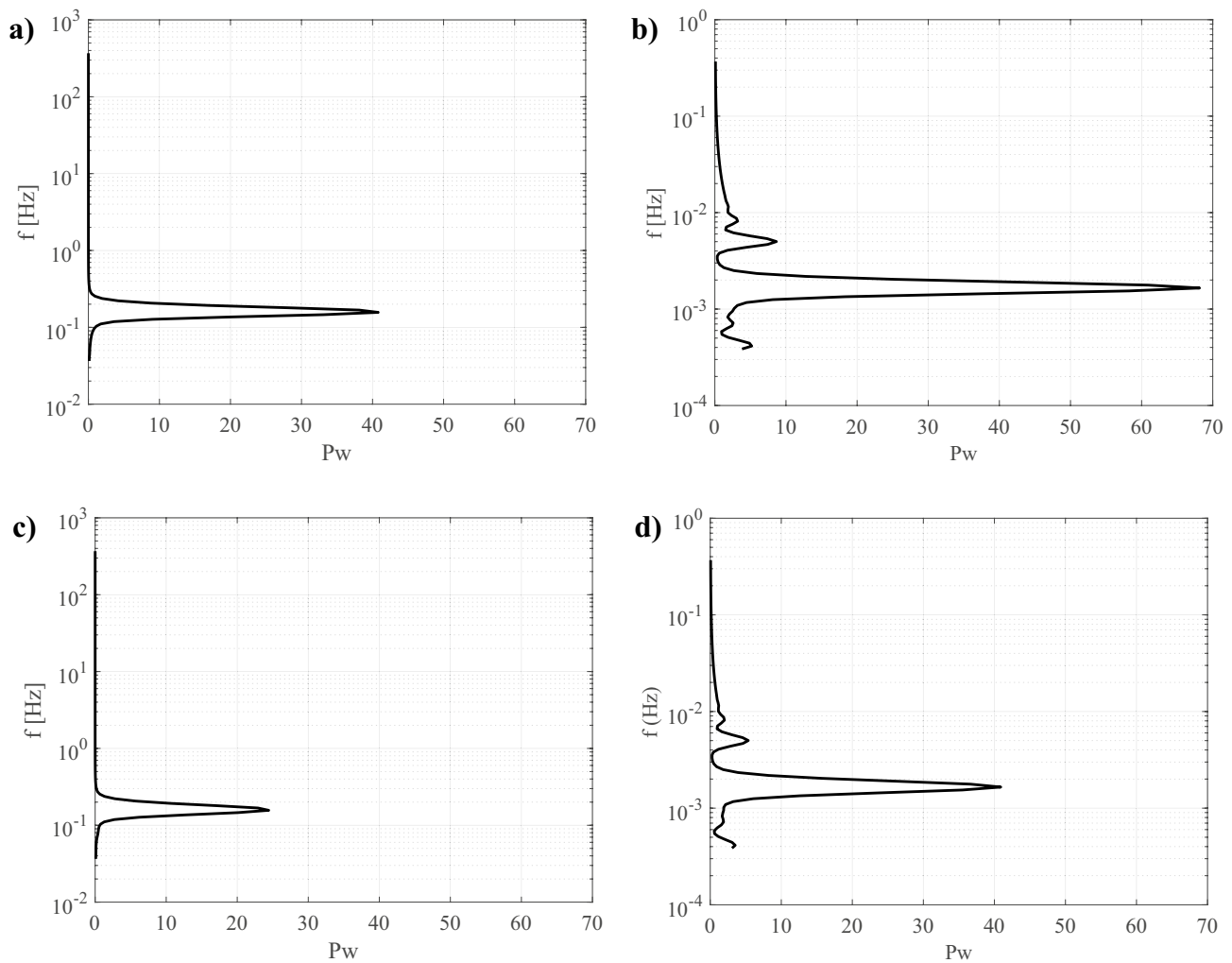
Fig. 5 Power spectra: **a**) sine function; **b**) square wave; **c**) sine function with two different amplitudes; **d**) square wave with two different amplitudes

the entire device. The changes in the trend in thermal behavior may be explained by the variations in the distribution of vapor bubbles and liquid slugs, which are usually called flow patterns. Typically, a slug flow, a semi-annular or an annular flow, can be found in PHPs, and according to flow patterns and working regimes, the PHP performance differs [41].

To better investigate the influence of the flow patterns and working regimes, temperature distributions obtained with the infrared camera in the condenser area at diverse values of the heat input (i.e., 0.5 W, 3.7 W) are reported for the same value of the filling ratio (46%) for different time points (Fig. 8). It can be observed from the infrared maps on the left-hand side of Fig. 8 that for a heat power of approximately 0.5 W, pulsating phenomena only began in some turns and were feeble wherever they appeared. The increase of temperature with respect to the ambient temperature that occurs in some of the turns is due to the first moving of fluid promoted by the increase of pressure at the evaporator and to

the initial weak evaporative phenomena. This behavior could be ascribed to the beginning of the startup regime, which will reach full operating mode with the increasing power at the evaporator. This supposition is confirmed also by the data presented in Fig. 7, which shows the global thermal resistance of the device. It may be noticed that 0.5 W could represent the transition value between a regime in which the heat exchange is principally due to the conduction within the fluid to a regime in which oscillating phenomena play the main role in the heat transfer. Indeed, for 0.5 W, there is a knee in the thermal resistance curve denoting the presence of regime transition.

Otherwise, the right-hand side of Fig. 8 shows that for a heat power of approximately 3.7 W, the pulsating phenomena are involved nearly all of the turns and are significantly more powerful than those observed at a heat power of 0.5 W. It is clearly visible that all the turns are activated and that the device is operating in full oscillation mode; pulsating
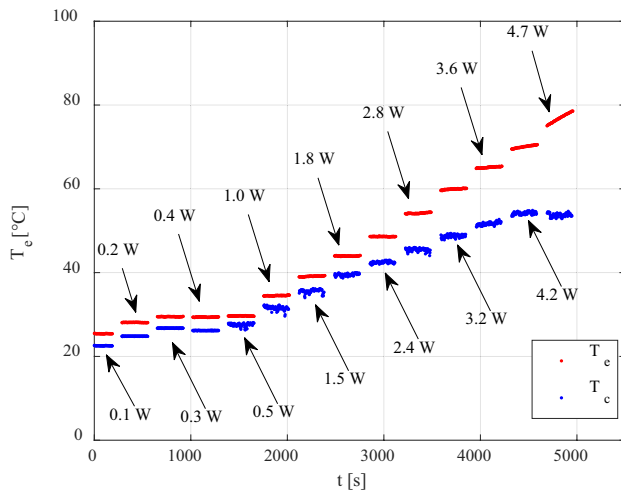
Fig. 6 Evaporator and condenser temperatures ($FR=46\%$)

phenomena can be perceived as the ascending movement from the heating section of heated fluid (i.e., turns 3,4,5) or as the descending movement of cooled fluid from the condenser (i.e., turns 2,7). The full activation of the device is confirmed by the global thermal resistance, showing that for a heat power of 3.7 W has already reached an asymptotic trend (Fig. 7).

However, the fact that some turns present a limited motion (i.e., turn 1) underlines the fact that characterizing the PHP thermal behavior and acquiring temperatures with few sensors, as it is widely performed, could be highly unreliable, due to dependence of the temperature values on the probes' location, even when the device is fully activated. This problem becomes more and more critical as the heat
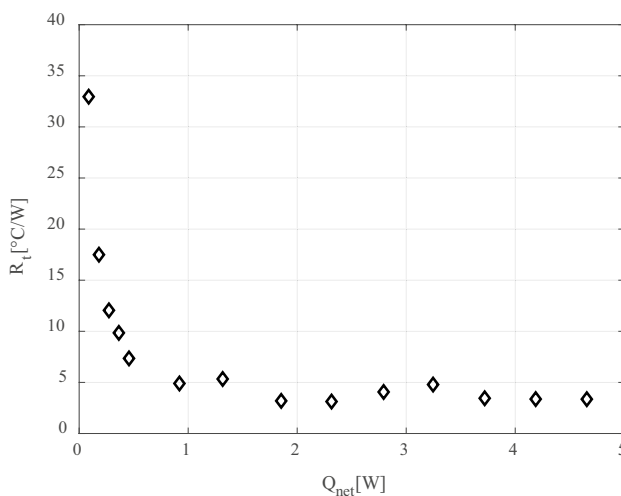
Fig. 7 Thermal resistance of the micro-PHP as a function of the heat power ($FR=46\%$)

power decreases and in correspondence with the transition between different working regimes.

The impact of the filling ratio on the thermal resistance of the micro-PHP is presented in Fig. 9. It can be observed that the $FR=46\%$ and $FR=82\%$ provide the best and the worst performance, respectively. These findings can be explained by considering that, for a high filling ratio, the micro-PHP almost works as a thermosyphon, because there are not enough bubbles to pump the fluid and because its motion is based on natural convection. On the other hand, when the filling ratio is too low (i.e., $FR=30\%$), oscillating slug flow is no longer preserved, because the liquid is insufficient.

For $FR=30\%$, it was also observed that at a heating power exceeding 1.3 W, thermal resistance begins to increase, probably due to the appearance of the first signs of dry-out at the evaporator, as confirmed by the analysis of infrared images presented in Fig. 10. For a heating power lower than 1.3 W (Fig. 10a), pulsating phenomena were still observed; whereas, for $Q_{net}=2.3$ W (Fig. 10b) all of the turns are rapidly increasing in temperature since the working regime is leaving the oscillating mode and approaching the dry-out. In this condition, most of the liquid is already evaporated: the vapour increases in temperature rapidly, and the remaining liquid becomes progressively less. Although the temperature ultimately reached was lower than the limit temperature of the device, this evidence was a clear indicator that the condenser was filled with vapor and that a rapid increase in the condenser temperature was expected. Therefore, the thermal characterization of the device for the cases of $FR=30\%$ and $FR=82\%$ was interrupted at lower values of power input than for the case $FR=46\%$ for security reasons; once the dry-out condition is approached, the increase in temperature and consequently in pressure is extremely steep and may compromise the integrity of the device.

To provide a comparison with the purely conductive mode, the empty micro-PHP was also tested. For $FR=0\%$, the thermal resistance of the micro-PHP was 36.2 °C/W; therefore, as compared with the micro-PHP at a filling ratio of zero, the thermal resistance at the optimal filling ratio (≈ 4 °C/W for $FR=46\%$) was approximately 10 times lower.

Since the analysis of the temperature distributions at the condenser revealed a different behavior for the various turns, the thermal resistance of each turn was evaluated. The condenser temperature was evaluated by averaging the temperature measured by infrared camera in each turn.

Figure 11 presents the thermal resistance of each turn as a function of the heat power for the optimal filling ratio (i.e., $FR=46\%$). The values referring to the single turns are characterized by a non-negligible variation, confirming that in order to describe the PHP thermal behavior, acquiring temperatures with few sensors may be quite deceptive. Therefore, the adoption of infrared measurements is a promising
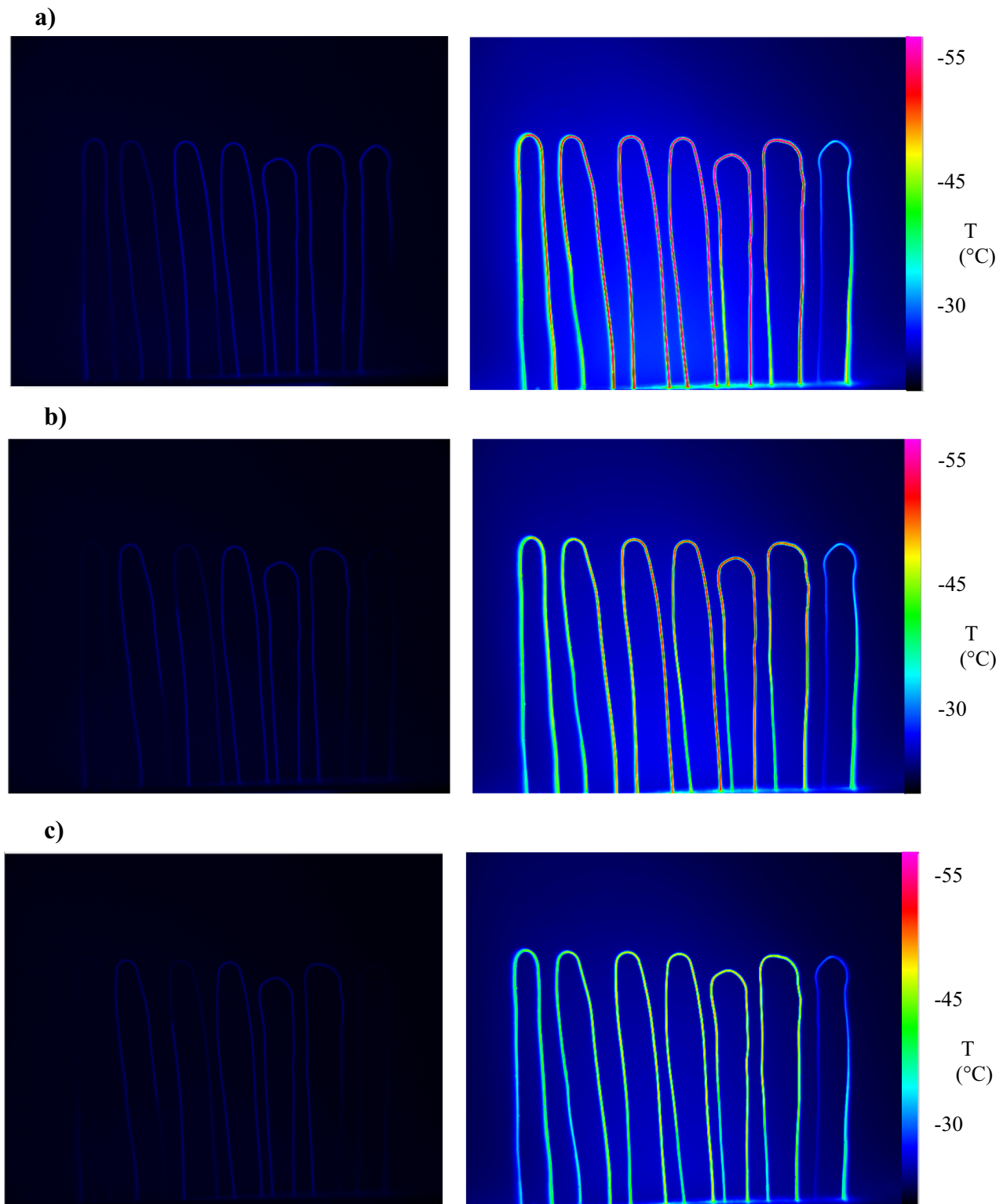
Fig. 8 Representative maps of the condenser temperature for $Q_{net}=0.5$ W (left-hand side) and $Q_{net}=3.7$ W (right-hand side) at various time-points ($FR=46\%$): **a)** $t=20$ s; **b)** $t=90$ s; **c)** $t=180$ s

solution that allows the accurate mapping of the temperature of the device. Referring to the details of the temperature distributions reported in Fig. 11b, it can be observed that the turns 2–6 present a discrepancy within 10–50%, while
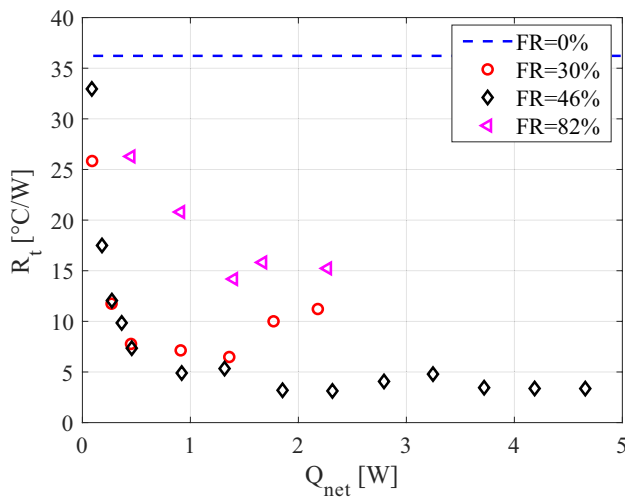
Fig. 9 Thermal resistance of the micro-PHP as a function of the heat power for different filling ratios

the turns 1 and 7 show, in many cases, values 100–200% higher than those of the other turns. The different behavior of these turns could be related to the valve attached to turn 1 and the horizontal tube joined to turn 7 performed like a cold liquid tank, partially inhibiting the oscillating motion. This difference is also present for the other filling ratios (Fig. 12), highlighting once again the importance of a significant number of points of measure to accurately characterize the performance of the device. This issue becomes increasingly relevant the device is characterized by small dimensions, because, as when analyzing the micro-PHPs, this problem is accompanied by temperature distortion from the presence of the sensors, which consequently affects the working behavior of the device.

To assess the effectiveness of the micro-PHP in our study, a comparison with other heat pipes was carried out. To account for the reduced size of the PHP currently under study, the heat transfer per unit volume was evaluated. It must be noted that because the thermal performance of the PHPs depend on many factors, the comparison only

considered the studies on heat pipes cooled by natural convection. In particular, the performance of the micro-PHP investigated in our study was compared with the performance of a PHP with an outer diameter of 4 mm [42] and of heat pipes with an outer diameter of 3 mm characterized by two different wick structures [43].

The comparison considered the thermal resistance of the heat pipe device (i.e. micro-PHP, PHP, wicked heat pipes) and a reference thermal resistance, which was evaluated by assuming that the whole heat transfer device was composed exclusively of a solid conductor made of copper; this was considered the best solution for heat conduction. Therefore, to estimate the heat transfer enhancement due to the adoption of this kind of two-phase device, an efficiency parameter, defined as the ratio, was calculated as follows:

$$\varepsilon = \frac{R_{ref}}{R_t} \tag{6}$$

where R_t is the average thermal resistance of the heat pipe device and R_{ref} denotes the reference thermal resistance, which was evaluated as follows:

$$R_{ref} = \frac{L}{\lambda A} \tag{7}$$

where L is the length of the solid conductor made of copper (i.e., the average distance between the evaporator and the condenser) and where λ and A represent the thermal conductivity and the total cross-sectional area of the solid conductor, respectively. It must be highlighted that the comparison considered the ratio between the reference thermal resistance and the average heat pipe's thermal resistance, because this ratio represents the heat transfer enhancement related to the adoption of the heat pipe technology; particularly, a high value of ε implies that the thermal resistance of the heat pipe technology is smaller than that of the heat conduction. Therefore, this parameter may be quite useful when comparing the thermal performance improvement that different technologies can provide.

Fig. 10 Maps of the condenser temperature at different heat inputs (*FR*=30%): **a)** Q_{net}= 0.9 W; **b)** Q_{net} = 2.3 W
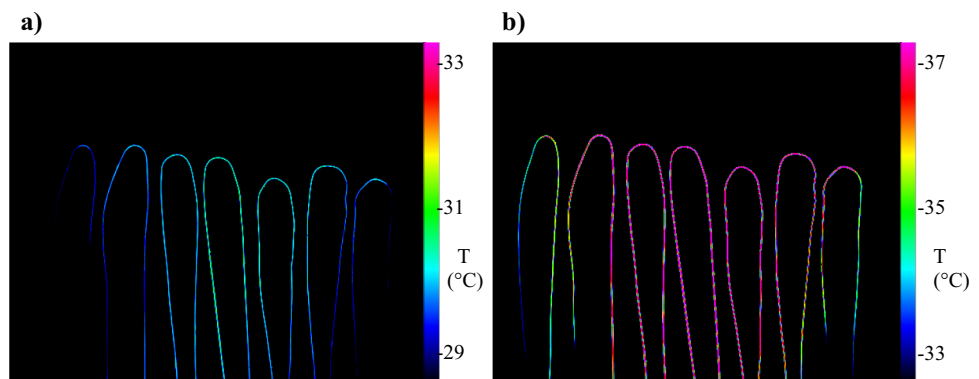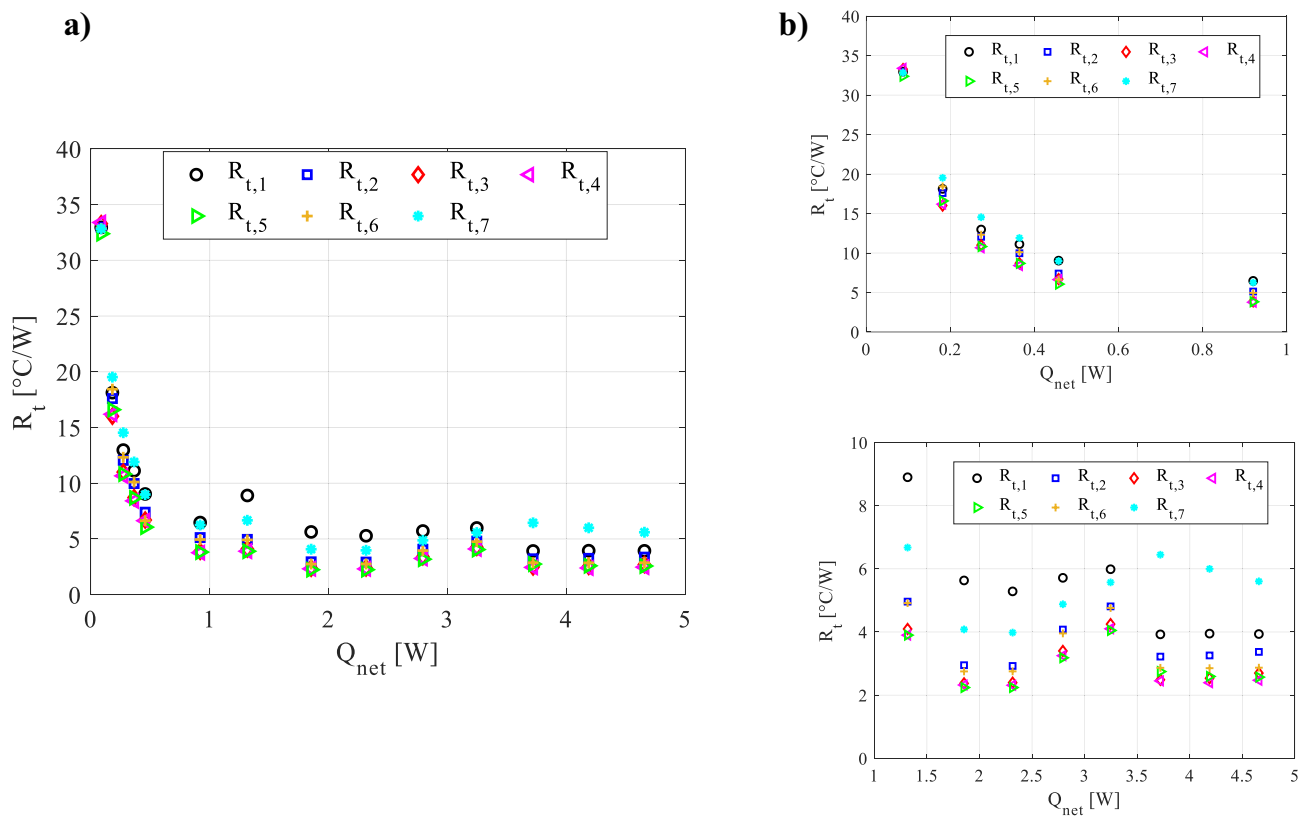
Fig. 11 **a**) Thermal resistance of each turn as a function of the heat power ($FR = 46\%$); **b**) two enlarged views of the distributions.

Table 1 shows that the micro-PHP investigated in our study is a promising technological solution, showing the highest values of ε. However, it must be noted that the thermal behavior of this kind of device depends on several factors; therefore, this parameter of merit is a useful marker of the good thermal performance of the device. Nevertheless, it cannot be the only factor evaluated.
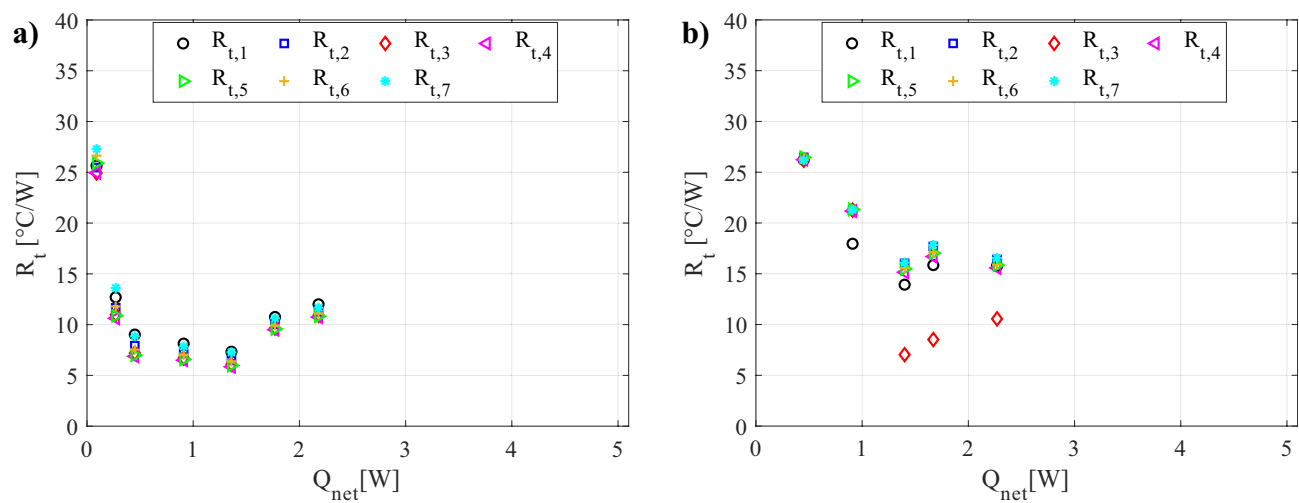
Fig. 12 **a**) Thermal resistance of each turn as a function of the heat power for $FR = 30\%$; **b**) $FR = 82\%$.

Table 1 Comparison between different heat pipe technologies

	Micro-PHP	Circular PHP [42]	Circular HP with fiber + spiral or powder metal [43]	Circular HP with mesh or groove [43]
ε	199	32	23	39

4.2 Frequency analysis

The analysis of the fluid pulsation frequency is essential to comprehend the principal mechanisms that govern PHP behavior given that its performance is strictly dependent on thermally induced pulsations.

The fluid oscillations from the heating section to the cooling section are characterized by a wide frequency spectrum, because a high degree of chaoticity is typical of the thermofluidic behavior of the PHP [24]. Consequently, the fluid pulsation frequency in this type of device is generally identified by a peak in the power spectrum (i.e., dominant frequency) of a specific dataset. To investigate the oscillation frequency, wavelet analysis was performed as described in Sect. 3.2, on the condenser temperature acquired by infrared camera. The analysis was focused on central turns (i.e., 3–5 turns) to avoid boundary effects from the presence of the valve and the horizontal pipe, as previously discussed. The analysis was focused on the filling ratio that guarantees the best performance (i.e., 46%).

Figure 13 presents some representative temperature signals measured by the infrared camera with an acquisition frequency of 18 Hz. These signals were obtained for one axial position of turn 4 in correspondence with the condenser. For a heating power of 0.5 W, only intermittent phenomena could be observed. For heating powers exceeding 1.3 W, a persistent oscillatory field was observed, changing with the increasing heating power.

The frequency analysis of temperature maps acquired by infrared camera allows for a wide and comprehensive analysis of the thermal oscillations occurring in the entire device. This solution represents a fascinating alternative to the classical methods to investigate the pulsations that characterize the motion in these devices overcoming the technical limits of the usually adopted techniques as previously stated.

The results of the scalograms are reported in Fig. 14. By analyzing the scalograms, it is possible to evaluate the local energy content of the temperature signal as a function of the frequency at every instant. Figure 14a (0.5 W) shows low characteristic frequencies, where the characteristic frequency corresponds to the time needed for a vapor plug and neighboring liquid slug to flow across a certain surface portion [22]. Indeed, the pulsating behavior at this low heat input can be described by frequency values around 0.05 Hz,

which is also confirmed by the data shown in Fig. 13a, in which the local temperature measurements show only intermittent oscillating behavior. This low frequency, as observed by Xu and Zhang [22] and by Mameli et al. [24], may be explained as that the liquid slugs distributed in the pipes are long at the lower heating power and that the fluid movement is very weak, and principally related to the coalescence of the smaller vapor plugs establishing a slug flow with a limited pulsation amplitude. It could be interpreted as the first signs of the beginning of the start-up regime.

At higher heat inputs, the presence of vertical peaks can be seen in the scalogram; these peaks correspond to pulsations with high energy content coming from the evaporator that swiftly crosses the condenser section. At first, these occasional high frequency and high energy peaks are grafted into a substrate with significantly lower characteristic frequencies; then, with the further increasing of the heating power given at the evaporator, the high frequency pulsating phenomena progressively rise in both number and energy. For $Q_{net} = 1.3$ W, it is possible to observe (Fig. 14b) that significant pulsating phenomena at high frequencies are not isolated events, since many peaks can be observed in the scalogram. However, even at this heat input, the characteristic frequencies fall in the low-value range, which means that even if high frequency pulsations can be detected, the oscillating motion is characterized by dominant low frequency phenomena, as the high energy area (red color) in the scalogram indicates. It probably means that fluid oscillation becomes more vigorous, yet plugs and slugs remain unevenly distributed within the device; therefore, a persistent oscillatory field is not yet observable. For higher values of heat power provided at the evaporator, the energy content of the temperature signal moved gradually from low to high frequency values. For 1.9 W and 2.3 W, two main classes of phenomena are observed. Oscillations characterized by a frequency of approximately 1 Hz that overlap a global pulsating behavior with a frequency of approximately 0.1 Hz that is no longer observable for higher heat input values (i.e., 3.7 W and 4.7 W).

The disappearance of low frequency phenomena indicates that the oscillation of the fluid in the branches has the same characteristic frequency that rises progressively along with increasing heat power. The pulsating flow can be deemed quasi-periodic, implying that the vapor plugs and liquid slugs are quasi-evenly diffused in the tubes at higher heating powers. It means that higher heat inputs create a more regular distribution of the vapor plug and the liquid slug [22].

To quantify the dominant pulsations frequencies of the analyzed oscillatory phenomena, the power spectrum, which indicates the signal power as a function of the frequency, was
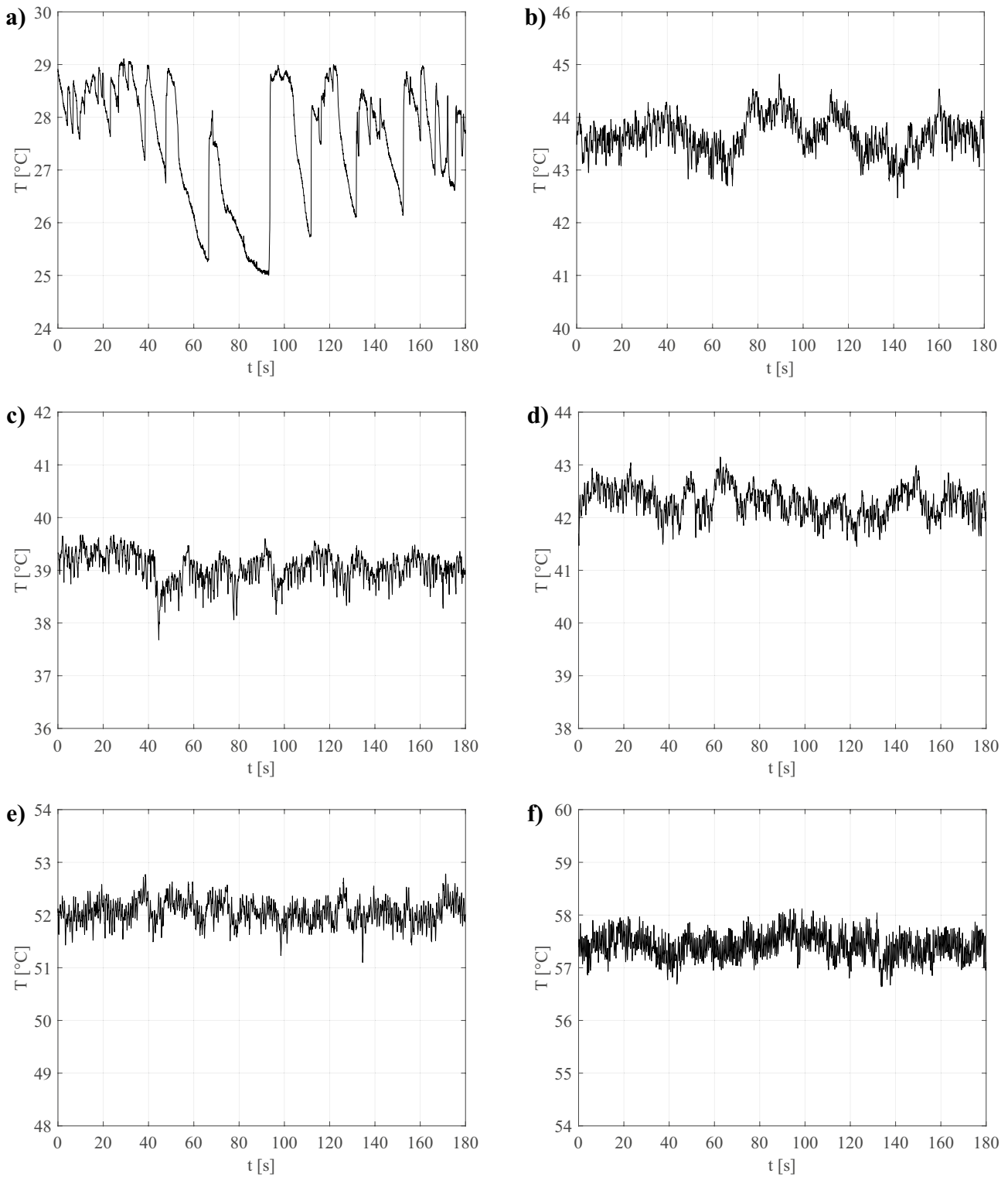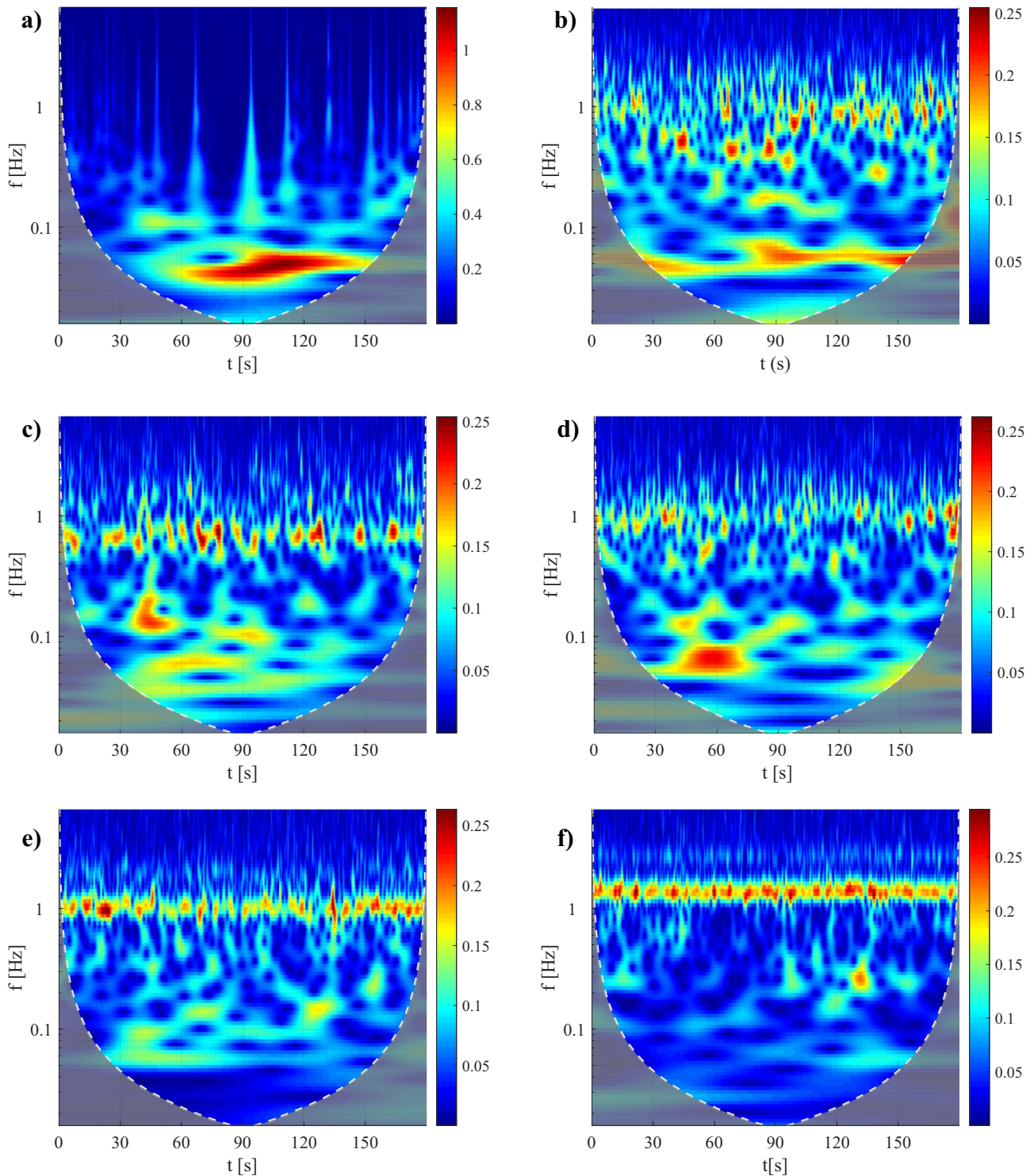
Fig. 13 Temperature signals for turn 4 ($FR = 46\%$): **a**) $Q_{net} = 0.5$ W; **b**) $Q_{net} = 1.3$ W; **c**) $Q_{net} = 1.9$ W; **d**) $Q_{net} = 2.3$ W; **e**) $Q_{net} = 3.7$ W; **f**) $Q_{net} = 4.7$ W

also evaluated. The power spectrum results are presented in Fig. 15. For $FR = 46\%$, the dominant frequencies fell in the range of 0.05–1.6 Hz. As observed in Fig. 14, for low

power input, the pulsating phenomena can be described by low frequency values ranging from 0.06–0.08 Hz (Fig. 15a, b). Moreover, the pulsation for 0.5 W can be completely

Fig. 14 Scalogram for turn 4 ($FR=46\%$): **a)** $Q_{net}=0.5$ W; **b)** $Q_{net}=1.3$ W; **c)** $Q_{net}=1.9$ W; **d)** $Q_{net}=2.3$ W; **e)** $Q_{net}=3.7$ W; **f)** $Q_{net}=4.7$ W

described by the dominant frequency, as shown by the isolated climax in Fig. 15a. For 1.3 W, an additional characteristic frequency is present at approximately 1 Hz and can describe the peaks observed in Fig. 14b.

As the heat power increases, the dominant frequency settles to values of approximately 1 Hz. As seen in the scalograms, there remain significant phenomena characterized by low frequency values, as indicated by the
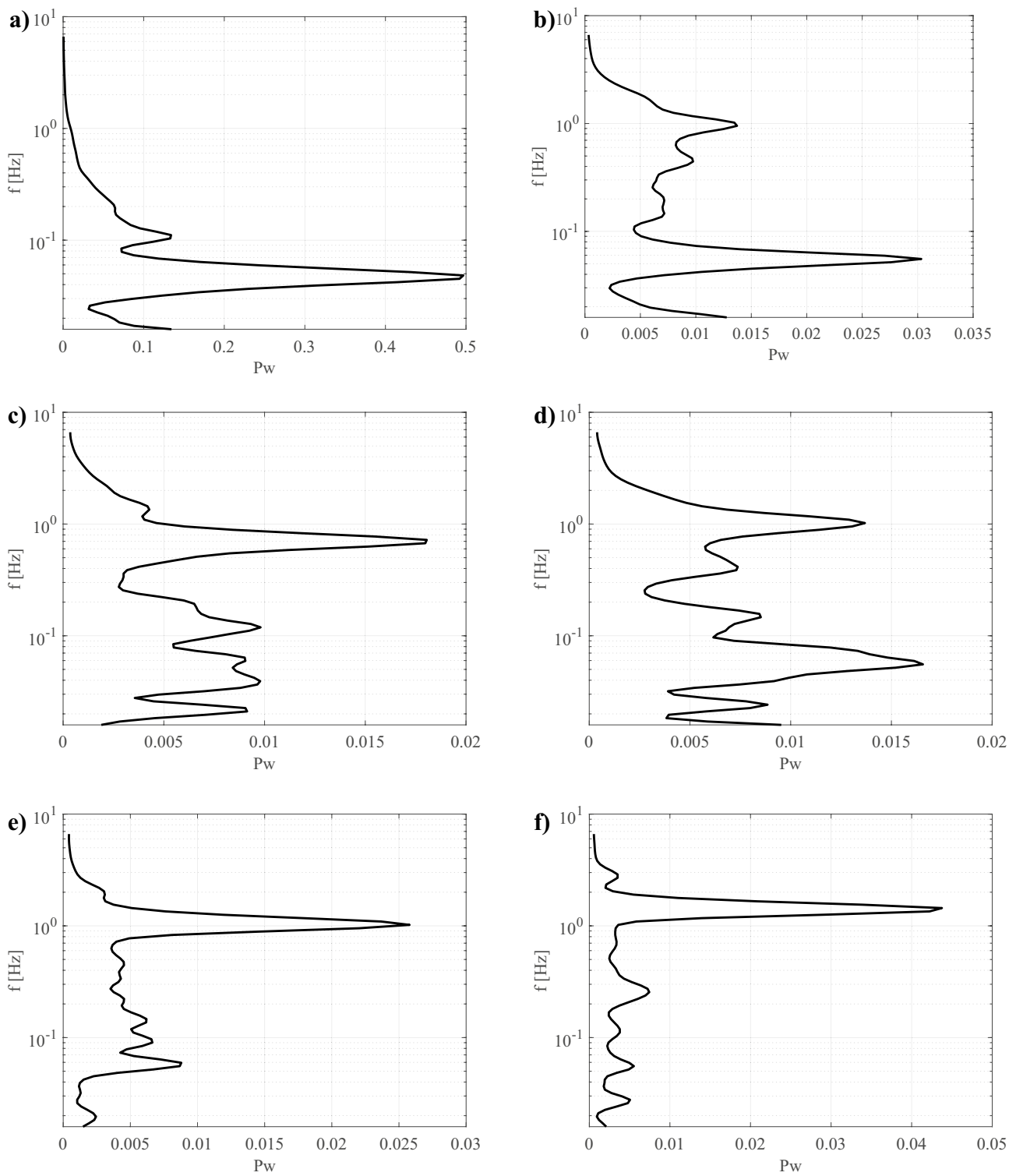
Fig. 15 Power spectrum for turn 4 (*FR* = 46%): **a)** Q_{net} = 0.5 W; **b)** Q_{net} = 1.3 W; **c)** Q_{net} = 1.9 W; **d)** Q_{net} = 2.3 W; **e)** Q_{net} = 3.7 W; **f)** Q_{net} = 4.7 W

multiple characteristic frequencies revealed by the different peaks (Fig. 15c, d). These peaks progressively diminish along with increasing heat power until they disappear

for 3.7 W. Moreover, globally, the dominant fluid pulsation frequency rises along with heating load. The results presented in Figs. 14 and 15 refer to a single turn (i.e., turn 4).
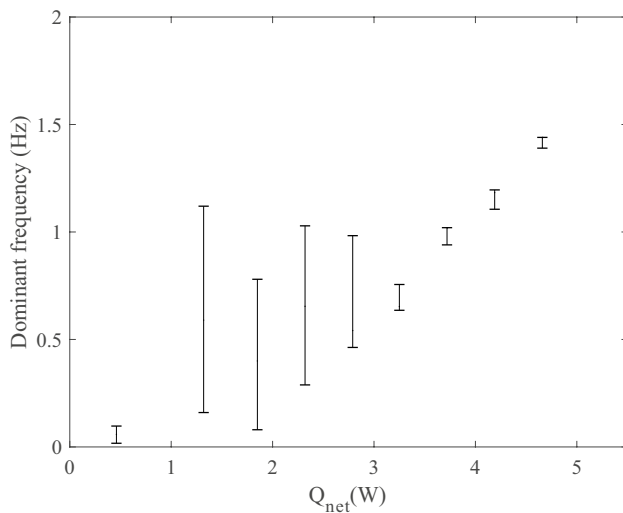
Fig. 16. 95% confidence intervals of dominant frequency values for the entire device as a function of heat power input (*FR* = 46%)

Therefore, in order to verify the repeatability of the oscillating behavior along the entirety of the device, we must replicate the analysis described above for the temperature signals of all of the turns.

The results of the dominant frequency for the entire device are presented in Fig. 16. For Q_{net} = 0.5 W, low frequency oscillations can be seen in all of the turns in the range of 0.02–0.1 Hz, which confirms what was hypothesized from the analysis of the infrared maps (Fig. 13) and of the scalograms (Fig. 14). These data could represent the first signs of the beginning of the start-up regime. At the power input of 1.3 W, the various turns share the two phenomena observed from the power spectrum; high-frequency pulsations (1 Hz) are present in some of the turns, while the low frequency phenomena from the power spectrum and the scalogram shows that the main role in the oscillating motion is found in the rest of the turns. This intermittent oscillating behavior is observable until the input power value has reached 2.3 W.

The wide confidence intervals observed for low power inputs denote that the turns are characterized by different values of dominant frequency and indicate a non-negligible variance in the fluid's movement over the entire PHP and the instability of the pulsations, which indicates only a partial activation of the device. The fluid oscillations show a higher repeatability within the entire PHP as the power input increases, as can be seen from the reduced confidence intervals; these results denote full activation of the PHP.

Indeed, for power input values exceeding 2.8 W, the fluid in all of the turns oscillates at the same dominant frequency indicative of a rising tendency with the heat load. This result proves that the PHP is fully activated and characterized by a quasi-uniform distribution of the vapor plugs and liquid slugs.

Similar frequency values were obtained by other researchers who investigated the dominant frequency in other kinds of PHPs and with other data processing techniques (Table 2). Although the devices investigated in the studies reported in Table 2 in some cases differ substantially to the one analyzed in our study, further comparisons may prove fruitful, since it highlights that even if the structure of these PHPs vary, their oscillating behavior in terms of dominant frequencies is comparable.

Cumulatively, our results highlight that the approach we have proposed herein can provide worthy evidence about the fluid motion inside the PHP.

Table 2 Literature analysis scheme

Authors name	Year	Geometry Cross-section	I.D./O.D [mm]	Turn	Working fluid	Signal	Type of Analysis	Frequency [Hz]	Heat input
Kim et al. [44]	2003	Square	1.5×1.5	10	R-142b	Fluid pressure	Fast Fourier Transform	1–2	0.6 – 0.9 W/cm²
Monroe et al. [45]	2017	Tubular	3.25/4.8	4	water	Fluid and wall temperature	Short-Time Fourier Transform	0.5–4	25–300 W
Suzuki [46]	2003	Tubular	2/3	4	water	Wall temperature	-	1–2	50–300 W
Ishii et al. [47]	2019	Square	2×2	12	water	Fluid temperature	Fast Fourier Transform	2	316 W
Das et al. [48]	2010	Tubular	2	1	pentane	Fluid pressure	-	2.5–4.2	-
Spinato et al. [49]	2015	Flat	1	1	R245fa	Wall temperature	Time Strip Technique	0.6 – 1.2	8 – 34 W
Khandekar et al. [50]	2009	Tubular	2/4	1	ethanol	Fluid pressure	Fast Fourier Transform	0.1–3	20 W

5 Conclusions

A micro-PHP fabricated with extra-thin metallic tube with an inner diameter of 0.32 mm and charged with HFC-134a has been experimentally investigated.

To characterize the performance of the tested micro-PHP, several heating powers and filling ratios were investigated. To highlight the different thermal behavior of each turn, an infrared camera was used to acquire the local temperature distributions on the wall of the entire PHP. To thoroughly study the pulsating behavior of the proposed PHP, the dominant frequencies were investigated by wavelet analysis.

The main research outcomes are:

- The best average performance can be reached for a filling ratio of 46% and for a heat input ranging between 1.9 W and 4.7 W.
- Two oscillating flow regimes are identified: non-persistent oscillating flow (high variance of the fluid oscillation in time and in space) and quasi-periodic oscillating flow (permanent and uniform fluid oscillation within the entire PHP).
- The fluid oscillation frequency analysis permits the detection of the PHP working regimes, depending on the power input provided to the evaporator. During the non-persistent oscillating flow ($Q_{net} < 2.3$ W), only some channels present fluid oscillations, and the turns are characterized by different values of dominant frequency (0.05–0.6 Hz); conversely, the dominant frequency for high power input to the evaporator (2.8–4.7 W) is generally similar in the whole condenser section and falls within the 0.6 – 1.5 Hz range. The device shows a complete activation.

In conclusion the results highlight that the here proposed approach can provide worthy evidence about the fluid motion inside the PHP allowing to overcome the limits introduced by the adoption of transparent materials for the direct flow visualization or by the invasive insertion of pressure sensors, particularly in devices with so small dimensions.

References

1. Murshed SMS, De Castro CN (2017) A critical review of traditional and emerging techniques and fluids for electronics cooling. Renew Sust Energ Rev 78:821–833
2. Chen Z, Li Y, Zhou W, Deng L, Yan Y (2019) Design, fabrication and thermal performance of a novel ultra-thin vapour chamber for cooling electronic devices. Energ Convers Manage 187:221–231
3. Ma H (2015) Oscillating heat pipes. Springer, Berlin
4. Faghri A (2014) Heat pipes: review, opportunities and challenges. Frontiers in Heat Pipes 5:1
5. Nazari MA, Ahmadi MH, Ghasempour R, Shafii MB, Mahian O, Kalogirou S, Wongwises S (2018) A review on pulsating heat pipes: from solar to cryogenic applications. Appl Energy 222:475–484
6. Bastakoti D, Zhang H, Li D, Cai W, Li F (2018) An overview on the developing trend of pulsating heat pipe and its performance. Appl Therm Eng 141:305–332
7. Hao T, Ma H, Ma X (2019) Heat transfer performance of polytetrafluoroethylene oscillating heat pipe with water, ethanol, and acetone as working fluids. Int J Heat Mass Tran 131:109–120
8. Taft BS, Williams AD, Drolen BL (2012) Review of pulsating heat pipe working fluid selection. J Thermophys Heat Tr 26(4):651–656
9. Cattani L, Mangini D, Bozzoli F, Pietrasanta L, Michè N, Mameli M, Filippeschi S, Rainieri S, Marengo M (2019) An original look into pulsating heat pipes: Inverse heat conduction approach for assessing the thermal behaviour. Thermal Science and Engineering Progress 10:317–326
10. Iwata N, Ogawa H, Miyazaki Y (2016) Maximum Heat Transfer and Operating Temperature of Oscillating Heat Pipe. J Heat Transf 138(12):122002
11. Iwata N, Ogawa H, Miyazaki Y (2011) Temperature-controllable oscillating heat pipe. J Thermophys Heat Tr 25(3):386–392
12. Iwata N, Miyazaki Y, Ogawa H (2018) Thermal Performance of Extra-thin Oscillating Heat Pipe. Joint 19th IHPC and 13th IHPS, Pisa, Italy, June 10–14, 2018
13. Bonfiglio C, Bozzoli F, Cattani L, Iwata N, Rainieri S, Vocale P (2020) Thermal Performance Investigation by Infrared Analysis of Mini Pulsating Heat Pipe. In Journal of Physics: Conference Series (Vol. 1599, No. 1, p. 012004). IOP Publishing
14. Yang KS, Cheng YC, Jeng MS, Chien KH, Shyu JC (2014) An Experimental Investigation of Micro Pulsating Heat Pipes. Micromachines 5:385–395
15. Yoon A, Kim SJ (2017) Characteristics of oscillating flow in a micro pulsating heat pipes: fundamental-mode oscillation. Int J Heat Mass Tran Transfer 109:242–253
16. Qu J, Wu HY, Wang Q (2012) Experimental Investigation of Silicon-Based Micro-Pulsating Heat Pipe for Cooling Electronics. Nanoscale Microscale Thermophys Eng 16(1):37–49
17. Yoon A, Kim SJ (2018) Understanding of the thermo-hydrodynamic coupling in a micro pulsating heat pipe. Int J Heat Mass Tran 127: 1004–1013
18. Kim J, Kim SJ (2020) Experimental investigation on working fluid selection in a micro pulsating heat pipe. Energ Convers Manage 205:112462
19. Jahani K, Mohammadi M, Shafii MB, Shiee Z (2013) Promising technology for electronic cooling: Nanofluidic micro pulsating

heat pipes. Journal of Electronic Packaging, Transactions of the ASME 135(2):021005

20. Lee J, Joo Y, Kim SJ (2018) Effects of the number of turns and the inclination angle on the operating limit of micro pulsating heat pipes. Int J Heat Mass Transf 124:1172–1180

21. Jun S, Kim SJ (2019) Experimental study on a criterion for normal operation of pulsating heat pipes in a horizontal orientation. Int J Heat Mass Tran 137:1064–1075

22. Xu JL, Zhang XM (2005) Start-up and steady thermal oscillation of a pulsating heat pipe". Heat and Mass Transfer/Waerme- und Stoffuebertragung 41(8):685–694

23. Fairley JD, Thompson SM, Anderson D (2015) Time–frequency analysis of flat-plate oscillating heat pipes. Int J Therm Sci 91:113–124

24. Mameli M, Marengo M, Khandekar S (2014) Local heat transfer measurement and thermo-fluid characterization of a pulsating heat pipe. Int J Therm Sci 75:140–152

25. Zhao N, Ma H, Pan X (2011) Wavelet Analysis of Oscillating Motions in an Oscillating Heat Pipe. ASME 2011 International Mechanical Engineering Congress and Exposition, IMECE 2011 10(PARTS A AND B), 545–549

26. Torrence C, Compo GP (1998) A Practical Guide to Wavelet Analysis. Bull Am Meteor Soc 79(1):61–78

27. Astarita T, Carlomagno GM (2012) Infrared Thermography for Thermo-fluid dynamics. Springer, Berlin

28. Bevington PR (1969) Data Reduction and Error Analysis for the Physical Sciences. McGraw-Hill, New York

29. Shafii MB, Faghri A, Zhang YW (2011) Thermal modeling of unlooped and looped pulsating heat pipes. J Heat Transfer 123:1159–1172

30. Perna R, Abela M, Mameli M, Mariotti A, Pietrasanta L, Marengo M, Filippeschi S (2020) Flow characterization of a pulsating heat pipe through the wavelet analysis of pressure signals. Appl Therm Eng 171:100622

31. Buresti G, Lombardi G, Bellazzini J (2004) On the analysis of fluctuating velocity signals through methods based on the wavelet and Hilbert transforms. Chaos, Solitons Fractals 20(1):149–158

32. Donald DA, Everingham YL, McKinna LW, Coomans D (2009) Feature selection in the wavelet domain: adaptive wavelets. Elsevier, 2009

33. Büssow R (2007) An algorithm for the continuous Morlet Wavelet transform. Mech Syst Signal Pr 21(8):2970–2979

34. Merry RJE (2005) Wavelet theory and applications: a literature study. DCT rapporten

35. Addison PS (2017) The illustrated wavelet transform handbook: introductory theory and applications in science, engineering, medicine and finance. CRC press

36. Nazari-Sharabian M, Karakouzian M (2020) Relationship between Sunspot Numbers and Mean Annual Precipitation: Application of Cross-Wavelet Transform. A Case Study. J Multidisciplinary Scientif J 3(1):67–78

37. Meyers SD, Kelly BG, O'Brien JJ (1993) An introduction to wavelet analysis in oceanography and meteorology: With application to the dispersion of Yanai waves. Mon Weather Rev 121(10):2858–2866

38. Qu J, Wu H, Cheng P (2012) Start-up, heat transfer and flow characteristics of silicon-based micro pulsating heat pipes. Int J Heat Mass Tran 55(21–22):6109–6120

39. Zhang XM, Xu JL, Zhou ZQ (2014) Experimental study of a pulsating heat pipe using fc-72, ethanol, and water as working fluids. Exp Heat Transfer 17(1):47–67

40. Han H, Cui X, Zhu Y, Sun S (2014) A comparative study of the behavior of working fluids and their properties on the performance of pulsating heat pipes (PHP). Int J Therm Sci 82(1):138–147

41. Marengo M, Nikolayev V (2018) Pulsating heat pipes: experimental analysis, design and applications. Encyclopedia of Two-Phase Heat Transf Flow IV 1–62

42. Cui X, Zhu Y, Li Z, Shun S (2014) Combination study of operation characteristics and heat transfer mechanism for pulsating heat pipe. Appl Therm Eng 65(1–2):394–402

43. Zohuri B (2016) Heat Pipe Design and Technology Modern Applications for Practical Thermal Management. 2nd Ed., Springer Nature, Switzerland, 2016

44. Kim JS, Bui NH, Jung HS, Lee W-H (2003) The study on pressure oscillation and heat transfer characteristics of oscillating capillary tube heat pipe. Korean Soc Mech Eng Int J 17(10):1533–1542

45. Monroe JG, Aspin ZS, Fairley JD, Thompson SM (2017) Analysis and comparison of internal and external temperature measurements of a tubular oscillating heat pipe. Exp Therm Fluid Sci 84:165–178

46. Suzuki O (2003) Heat-transport characteristics of a bubble-driven non-looped heat-transport device. Trans Japan Soc Mech Eng Part B 69(678):430–436

47. Ishii K, Fumoto K (2019) Temperature visualization and investigation inside evaporator of pulsating heat pipe using temperature-sensitive paint. Appl Therm Eng 155(5):575–583

48. Das SP, Lefevre F, Bonjour J, Khandekar S (2010) Parametric study of a two-phase oscillating flow in a capillary tube. In Proceedings of 15th International Heat Pipe Conference

49. Spinato G, Borhani N, Thome JR (2015) Understanding the self-sustained oscillating two-phase flow motion in a closed loop pulsating heat pipe. Energy 90:889–899

50. Khandekar S, Gautam AP, Sharma PK (2009) Multiple quasi-steady states in a closed loop pulsating heat pipe. Int J Therm Sci 48:535–546